Electrophoretic Deposition of Protective Spinel Coatings for Solid Oxide Cell Interconnects - Towards Stack Integration

Journal of The
Electrochemical Society

Electrophoretic Deposition of Protective Spinel Coatings for Solid Oxide Cell Interconnects – Towards Stack Integration

To cite this article: Martin Hilger *et al* 2026 *J. Electrochem. Soc.* **173** 034509

Journal of The Electrochemical Society, 2026 **173** 034509

Electrophoretic Deposition of Protective Spinel Coatings for Solid Oxide Cell Interconnects – Towards Stack Integration

Martin Hilger,[1,2] Thorbjørn Krogsgaard,[3] Sonja-Michaela Groß-Barsnick,[4] Doris Sebold,[1] S. Shrikanth,[3] Jan Froitzheim,[3] Christian Lenser,[1,z] and Norbert H. Menzler[1,2,*]

[1] *Forschungszentrum Jülich GmbH, Institute of Energy Materials and Devices, IMD-2: Materials Synthesis and Processing, 52425 Jülich, Germany*
[2] *RWTH Aachen University, Institute of Mineral Engineering (GHI), 52074 Aachen, Germany*
[3] *Chalmers University of Technology, Department of Chemistry and Chemical Engineering: Energy and Materials, SE—412 96 Göteborg, Sweden*
[4] *Forschungszentrum Jülich GmbH, Institute of Technology and Engineering, ITE, 52425 Jülich, Germany*

We evaluated electrophoretic deposition (EPD) of spinel coatings for solid oxide cell (SOC) interconnects with a focus on stack integration. Two compositions, $MnCo_{1.9}Fe_{0.1}O_4$ (MCF) and $CuMn_{1.8}Ni_{0.2}O_4$ (CMN), were deposited from water/ethanol suspensions and subjected to three thermal routes: direct oxidation and two-step treatments with reduction in Ar/H_2 at 900 or 1000 °C followed by oxidation. Structural evolution, chromium evaporation, mass gain, and ex situ area-specific resistance (ASR) were assessed. Sealant compatibility with a Ca-Ba-silicate glass and applicability to representative flow-field geometries were investigated. All coatings formed continuous layers; two-step treatments enhanced densification compared to direct oxidation. Prereduction of MCF layers at 1000 °C yielded the lowest Cr evaporation and mass gain, whereas CMN exhibited chromium ingress, phase variations, and coarsened microstructures. ASR values for all types remained around or below 20 mΩ cm^2. Glass-joining produced dense composites; limited cation diffusion was observed for MCF, while CMN showed substantial Cu penetration into the glass. EPD produced uniform, defect-free coatings on complex flow-field structures, with only slight thickness variations across the profile. These results support MCF-EPD with a 1000 °C reduction step and in situ oxidation during stack assembly as a process-compatible route for protective interconnect coatings in high-temperature SOCs, while CMN remains of particular interest for intermediate-temperature applications.

 [DOI: 10.1149/1945-7111/ae3ebb]

Manuscript submitted November 14, 2025; revised manuscript received January 23, 2026. Published February 12, 2026. *This paper is part of the JES Focus Issue on SOFC XIX: Advances in Solid Oxide Fuel Cell and Electrolysis Cell Technology.*

Supplementary material for this article is available online

The global energy transition requires efficient storage technologies and the large-scale utilization of renewable energy sources. In this context, hydrogen represents a key technology, indispensable particularly in sectors that are difficult to decarbonize by other means. Solid oxide cells (SOCs) are of particular relevance, as they combine exceptionally high efficiency—especially in combined heat and power applications—with reversible operation. These characteristics assign SOCs a special role within the portfolio of hydrogen technologies.[1–3]

Within an SOC stack, ferritic stainless steel interconnects are a key component since they are directly associated with some of the most critical degradation phenomena. These include excessive oxidation and the evaporation of volatile chromium species, which lead to performance losses of the air electrode ("Cr-poisoning"), as well as resistive chromia scale formation and, in extreme cases, break-away corrosion.[4–6] Interconnects are one of the main cost drivers of SOC stacks, leading to a conflict between stack cost and stack lifetime, which becomes limited by Cr-depletion (and ensuing Fe-oxidation) when using very thin interconnects. To ensure reliable long-term operation of SOC stacks, protective coatings that prevent Cr-evaporation and limit chromia scale formation on the air side of interconnects have therefore become indispensable.[7]

Protective coatings are required to fulfil a set of stringent criteria: chemical and mechanical stability under oxidizing SOC conditions, suppression of uncontrolled steel corrosion and chromium volatilization, compatibility in thermal expansion with both steel and ceramic cells, adequate electrical and thermal conductivity, and the formation of a continuous, defect-free layer.[8,9] Among the various materials investigated, Mn-Co spinels have been established as the state-of-the-art. Extensive research has been dedicated to optimizing their composition and dopant additions, leading to highly reliable coatings for SOC interconnects.[10] At Forschungszentrum Jülich, the Fe-doped $MnCo_2O_4$ composition ($MnCo_{1.9}Fe_{0.1}O_4$, MCF) has proven particularly robust, both in oxidation tests and in stack applications, where atmospheric plasma sprayed (APS) coatings demonstrated stability beyond 30,000 h of operation.[11] It has demonstrated excellent protective properties both in laboratory-scale studies using different deposition techniques and in long-term stack tests exceeding 30,000 h.[11–16] Reported material data include a CTE of 13.4 × 10^{-6} K^{-1} and an electrical conductivity of 72 S cm^{-1} at 800 °C.[17,18] In this work, MCF is therefore chosen as a benchmark composition.

However, the reliance on cobalt poses ecological, social, and economic challenges due to its scarcity and critical supply situation.[19,20] Therefore, Co-free alternatives have attracted growing attention, with Cu-Mn spinels being the most prominent candidate family. Similar to Mn-Co spinels, compositional tailoring and dopant additions play a decisive role in tuning the protective properties of Cu-Mn spinels. While undoped or Fe-doped Cu-Mn spinels generally lag behind Mn-Co spinels in terms of stability and protection, Basu and co-workers have reported substantial improvements through Ni incorporation. In particular, the composition $CuMn_{1.8}Ni_{0.2}O_4$ (CMN) has been highlighted for its favorable electrical and thermo-mechanical properties.[21–23] Building on earlier work on undoped Cu-Mn spinels—including the first application of EPD to such compositions by Huang et al. in 2008—the role of Ni as a dopant has been systematically studied.[24] Ni additions have been shown to improve stability, processability, and conductivity.[21–23,25] Zhu et al. reported an electrical conductivity of 100 S cm^{-1} at 800 °C for $CuMn_{1.8}Ni_{0.2}O_4$, compared to 75 S cm^{-1} for undoped $CuMn_2O_4$, identifying the chosen composition as the most suitable candidate among various Ni doping levels.[21] These studies also demonstrate the suitability of CMN coatings for processing via EPD. While no

*Electrochemical Society Member.
[z] E-mail: c.lenser@fz-juelich.de

explicit thermal expansion data are available for this exact composition, Ling and Petric reported a CTE of 11.6×10^{-6} K^{-1} for a closely related spinel and highlighted the overall compatibility of Cu-Mn spinels with SOC stack materials.[26]

Next to material selection, the coating method is equally decisive to fully exploit the material properties and to ensure consistent coating quality at an industrially relevant scale. APS remains the established deposition method at Forschungszentrum Jülich and relevant beyond, but it is associated with drawbacks such as high material consumption and large coating thicknesses.[12] Moreover, potential substrate damage, such as warpage, presents a significant risk resulting from the high particle velocities and temperatures during the process. These limitations become particularly critical for thin, lightweight interconnects, which are of increasing relevance for industrial applications. Electrophoretic deposition (EPD) offers a promising alternative, enabling thin, homogeneous coatings on complex geometries with minimal material and energy demand.[27] In addition, in the field of SOC interconnect research, Zanchi, Sabato and co-workers already successfully demonstrated the overall applicability of the EPD procedure on real-scale components.[27,28]

While extensive research has been conducted on protective coatings for ferritic interconnect steels, many studies necessarily focus on simplified sample formats and test environments that do not fully capture the complexity of real SOC stacks. However, the integration of coatings into the actual stack assembly remains a largely underexplored but critical aspect. The joining step of the stack, performed at Forschungszentrum Jülich under standardized conditions of 850 °C for 100 h, provides a representative environment for evaluating such integrability. During this process, the interconnect's air side is exposed to oxidizing conditions, while the fuel side remains in reducing atmosphere, minimizing oxidation. Importantly, this step offers the opportunity for the final densification of the coating to be realized in situ during stack joining itself. This approach not only eliminates the need for additional ex situ sintering steps in oxidizing atmospheres—which would otherwise expose uncoated zones such as sealing edges or fuel-side contact areas to undesired corrosion—but also represents a central conceptual advance of this study.

For EPD-applied spinel coatings, two-step thermal treatments with a reducing pre-treatment prior to final oxidation (reactive sintering) have previously been shown to achieve dense and adherent layers.[12,29–31] While such pre-reduction steps add complexity to the process chain, they are considered particularly beneficial for ensuring coating densification. At the same time, the lack of sufficient densification at the onset of the joining step may facilitate chromium release, which underlines the importance of carefully assessing this trade-off in the context of in situ integration.

The present study addresses this challenge by systematically evaluating two EPD-applied spinel coatings—MCF as benchmark and CMN as cobalt-free alternative—under three different thermal treatment programs: direct oxidation and two-step treatments with pre-reduction at 900 °C or 1000 °C. Particular attention is paid to the relevance of these treatments within the stack manufacturing context. The coatings are investigated with respect to their phase formation and microstructure, chromium retention capability, mass gain, and area-specific resistance (ASR). Their compatibility with glass sealants during stack joining is assessed, and the best-performing coatings are transferred onto two representative interconnect flow-field geometries—the Jülich F10 design with thick interconnects and the lightweight hydroformed CS^V-type—relevant for stationary and mobile SOC systems, respectively.

The specific objectives of this work can be summarized as follows:

- Evaluate the capability of in situ densification of EPD coatings during stack joining.
- Assess the suppression of volatile chromium species and overall oxidation behavior during stack assembly and subsequent stack start.
- Determine the electrical conductivity of the interconnect component by ex situ ASR measurements.
- Investigate the chemical and thermo-mechanical compatibility of coatings with glass sealants.
- Demonstrate the applicability of the coating process and thermal treatments to complex interconnect flow-field structures.

By linking coating performance directly to stack-relevant processing and integration aspects, this study aims to highlight the potential of EPD coatings to serve as efficient, scalable, and sustainable protective solutions for SOC interconnects.

Experimental

Materials.— *Stainless steel.*—All coatings investigated in this work were deposited on 0.3 mm thick steel sheets. For the evaluation of microstructural development as well as chromium evaporation and mass-gain behavior during 500 h of exposure, followed by post-exposure ASR measurements, Crofer22APU was employed. Crofer22H was chosen for assessing glass sealant compatibility. Finally, for investigations on real interconnect geometries, cut-outs from representative flow-field structures were used: (i) an established interconnect type machined from Crofer22APU bulk material, and (ii) a lightweight interconnect type manufactured by hydroforming Crofer22H sheets. The compositions of both grades, together with their coefficients of thermal expansion (CTE) at 800 °C, are summarized Table I.

Spinel powders.—For this study, two different sources of powders were used. Commercial MCF powder was obtained from KCeracell (Pyeongtaek, South Korea), whereas CMN powder was synthesized within the framework of the project NOUVEAU by Marion Technologies (Verniolle, France). Both powders were processed analogously prior to suspension preparation. Mechanical milling was performed to achieve a particle size distribution suitable for the EPD process, using a planetary ball mill (Pulverisette 7, manufacturer: Fritsch GmbH, Idar-Oberstein, Germany). In each run, 10 g of powder were milled in 25 ml ethanol with 100 g of YSZ balls (1 mm diameter) at 500 rpm for 1 h. After milling, the powders were separated from the solvent and dried, followed by gentle manual milling in a mortar to break up residual agglomerates.

Powder characterization included particle size distribution (PSD) analysis by dynamic light scattering (DLS), specific surface area (SSA) determination by gas adsorption, and morphology assessment by scanning electron microscopy (SEM). Particle size and morphology are decisive parameters for deposition behavior and coating quality in the EPD process. Detailed methodology of powder characterization is given in the characterization section on spinel powders.

Coating preparation.—The development of the coating approach, including optimization of powder preparation, suspension composition, and deposition parameters, was carried out prior to this study and is therefore not discussed in detail here. In the present work, coatings were deposited on two types of substrates: flat steel coupons for the fundamental characterization of coating properties and the determination of performance-relevant indicators, as well as substrates featuring flow fields (gas distribution structures), where minor adjustments to the deposition procedure were required.

For both spinel compositions, the processing route was applied in an analogous manner. This included the preparation of the green coatings as well as the subsequent use of identical thermal treatment protocols to achieve densification.

Electrophoretic deposition.—The EPD process was developed based on earlier studies by Smeacetto and co-workers employing mixed ethanol-water suspensions.[34–37] Suspension and deposition parameters were optimized beforehand on flat Crofer22APU

Table I. Chemical composition and CTE (at 800 °C) for Crofer22APU and Crofer22H.[32,33]

		Fe —	Cr wt%	C wt%	N wt%	S wt%	Mn wt%	Si wt%	Ti wt%	W wt%	Nb wt%	Cu wt%	P wt%	Ni wt%	Al wt%	La wt%	CTE 10^{-6} K^{-1}
Crofer22APU	min	Bal.	20.0	0.03	—		0.30		0.03	—	—			—		0.04	11.9
	max		24.0		—	0.02	0.80	0.50	0.20	—	—	0.50	0.05	—	0.50	0.20	
Crofer22H	min	Bal.	20.0	0.03				0.10	0.02	1.0	0.20					0.04	11.8
	max		24.0		0.04	0.006	0.80	0.60	0.20	3.0	1.0	0.50	0.50	0.50	0.1	0.20	

substrates with respect to coating homogeneity, defect minimization, and process practicability.

For all coatings, a suspension medium consisting of 60 vol% ethanol and 40 vol% deionized water was employed, ensuring sufficient particle charging without additional additives. The solid content was set to 40 g l^{-1}. Prior to suspension preparation, the powders were processed using a planetary ball mill and subsequently de-agglomerated manually with a mortar (see the materials section on spinel powders). For stabilization, the suspension was stirred magnetically for 30 min, followed by 30 min ultrasonication in a Sonorex Digitec bath (manufacturer: Bandelin, Berlin, Germany), with manual stirring for 1 min every 5 min.

Deposition was performed at a constant voltage of 40 V, applied by a three-channel laboratory power supply of type 2230-30-1 (manufacturer: Keithley Instruments, Solon, Ohio, USA). A parallel electrode configuration was used, with two flat Crofer22H counter electrodes positioned symmetrically at a distance of 15 mm from the substrate. For the microstructural characterization, glass-sealant compatibility tests, and investigations on flow-field structures, 25 mm × 25 mm coupons were coated. To obtain single-side coated samples, the rear surface of each coupon was covered by an uncoated steel sheet of equal size. For these experiments, 100 ml of suspension was used per deposition.

For chromium evaporation, mass-gain, and ASR investigations, perforated steel plates (approx. 5 cm × 10 cm) accommodating ten individual coupons of 15 mm × 17 mm were coated on both sides to minimize uncoated surface areas. The coated coupons were subsequently separated for testing (details in the characterization section on chromium evaporation). These depositions required 400 ml of suspension per batch.

The optimized deposition time was 45 s for flat substrates, independent of the substrate size. For flow-field structures, where the effective surface area is approximately one third larger compared to flat coupons, the deposition time was increased to 60 s to achieve comparable coating thicknesses and quality. After deposition, all samples were air-dried overnight at room temperature.

Thermal treatments.—After EPD and subsequent drying, the coatings are present in a non-densified state. Appropriate thermal treatments are therefore required to achieve densification, ensure adhesion to the underlying steel substrate, and generate a coherent layer with closed porosity, capable of effectively blocking inward or outward migrating O- and Cr-species.

At the same time, the thermal treatments are intended to be compatible with the thermal process chain of SOC stack fabrication. Each additional heat treatment step represents a hurdle in terms of scalability and cost, and partial coating of interconnect components requires careful consideration of uncoated areas such as sealing zones or the fuel side. In particular, the exposure of uncoated surfaces to oxidizing atmospheres must be avoided, as this would compromise the integrity of the interconnect and the functionality of contacting areas such as Ni meshes spot-welded on the fuel side.

To minimize such risks, the final densification of the coatings was targeted to occur in situ during the stack assembly step or early operation. At Forschungszentrum Jülich, the established stack assembly procedure involves a 100 h joining step at 850 °C, designed to ensure crystallization and toughening of the sealing glass.[38] This process is preceded by a three-step heating program applied at 2 K min^{-1}, with intermediate dwells at 350 °C and 550 °C, to enable gradual binder removal of the screen-printed glass seal and to ensure uniform heating of the components. During this joining step, the interconnects are exposed to air on the coating side, while argon gas is supplied on the opposite side, minimizing oxidation of the uncoated steel surface. A schematic of the joining procedure is shown in Fig. 1a.

For microstructural and phase analyses, a simplified oxidation program was used, applying a continuous heating rate of 5 K min^{-1}. In contrast, for chromium evaporation, mass gain, and sealant compatibility experiments, the full multi-step program was employed. Although a 100 h exposure at 850 °C represents a comparatively harsh condition—especially for Cu-Mn spinels—it remains the established standard in Jülich to guarantee reliable glass sealant crystallization and is therefore considered in the present study.

While the currently established APS-MCF coatings can be integrated into the stack without additional heat treatment, literature reports indicate that suspension-based spinel coatings benefit from two-step treatments including a preliminary reduction step, which promotes densification through so-called "reactive sintering." In this mechanism, partial reduction of the spinel and the transient presence of metallic phases enhance diffusion-driven sintering, leading to denser coatings with closed porosity.[29–31]

In the present study, the influence of such a reduction step was systematically assessed. Two different reduction programs were carried out for 2 h in Ar/2.9% H_2, with heating and cooling rates of 5 K min^{-1}, at 900 °C or 1000 °C, respectively. These were followed by an oxidation step, representing the stack joining procedure, resulting in three distinct programs: a single-step oxidation (S0), reduction at 900 °C followed by oxidation (R1/S1), and reduction at 1000 °C followed by oxidation (R2/S2). The selection of these programs was based on the established work by Wolff et al. on wet powder spraying of MCF,[16] a comprehensive review by Zanchi et al. on EPD-based interconnect coatings,[27] as well as findings from our own preceding work.[12] A schematic of the applied thermal protocols is provided in Fig. 1b.

Beyond the stack assembly, this study also considers the behavior of the coatings during the first several hundred hours of operation. Together with the simulated joining step, an additional 400 h exposure was carried out at 800 °C in air to evaluate the effectiveness of the coatings in suppressing chromium evaporation and oxidation, as well as the resulting ASR values. It should be noted that operation at 800 °C represents comparatively harsh conditions for CMN and Cu-Mn spinels in general. However, this temperature is still the established standard for higher temperature SOCs (e.g. with electrolyte-supported cells), whereas Cu-Mn spinels are often considered more suitable for intermediate-temperature SOC operation in the 600 °C–700 °C range.[21,22,25,39] Testing at 800 °C therefore provides an accelerated assessment, where degradation effects appear more rapidly but remain indicative of the long-term behavior expected under milder intermediate-temperature conditions. This emphasizes the particular focus on the durability of CMN coatings in the present study. A schematic illustration of the thermal treatment protocols, the stack joining, and the subsequent start-up exposure is presented in Fig. 1c).

Characterization.— *Spinel powders.*—For a comparative characterization of the powders in terms of particle morphology, size, and specific surface area, both qualitative and quantitative methods were applied. Morphologies were assessed by SEM, while particle size distributions and surface areas were determined by laser diffraction and gas adsorption, respectively.

SEM imaging was carried out using a GeminiSEM 450 and an Ultra 55 (manufacturer: Zeiss, Oberkochen, Germany) equipped with a field emission electron source. Secondary electron (SE) detection was applied to obtain topographic contrast and backscattered electron (BSE) detection served highlighting phase contrast. For imaging, the powders were dispersed on conductive carbon tape to ensure electrical conductivity and adhesion in the vacuum chamber.

PSD measurements were conducted with a laser diffraction particle size analyzer (LA-950V2, manufacturer: Horiba, Kyoto, Japan) operating at 405 nm and 650 nm laser wavelengths. Given the fine particle sizes, Mie theory was applied for evaluation, assuming a refractive index of 2.

Specific surface areas were determined via N_2 gas adsorption using an AREA-mat system (manufacturer: Jung Instruments, Viersen, Germany).

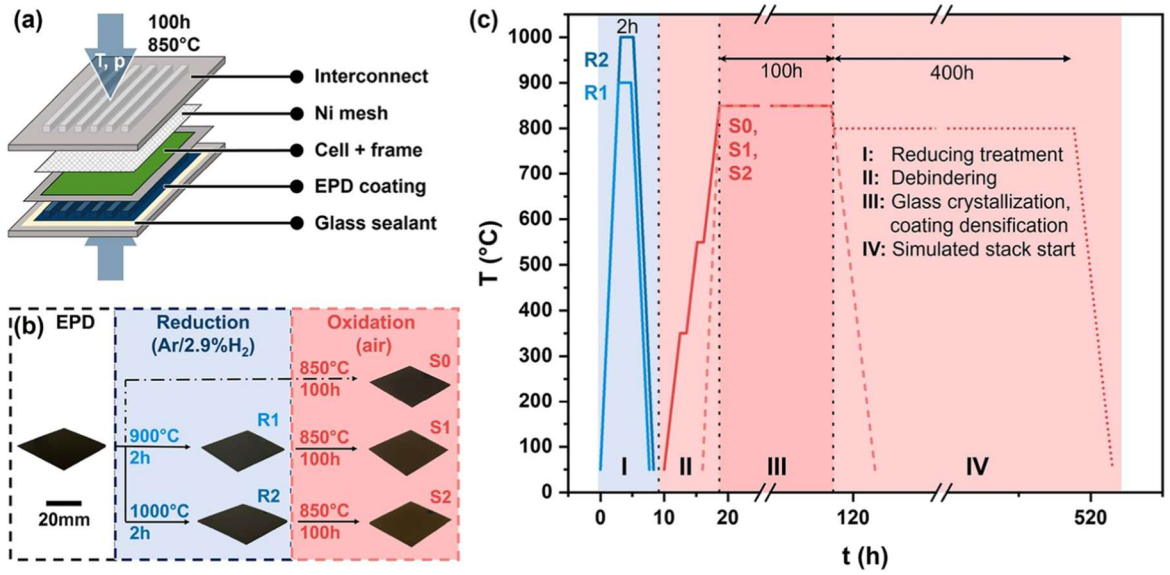

Figure 1. Stack-assembly procedure and related heat treatment protocols. (a) Schematic of a single repeating unit in SOC stack during joining step, (b) flow-chart of the three investigated treatments S0, S1 and S2, and (c) thermal history during heat treatments and testing within this study, indicating multi-step and shortened heating ramp within the stack assembly phase.

Evolution of phases and microstructures.—To assess the changes in the coatings and coated substrates along the processing steps investigated in this study, analyses were conducted at specific stages with respect to phase formation by X-ray diffraction (XRD) and to microstructures and elemental distributions by SEM and energy-dispersive X-ray spectroscopy (EDS). These investigations provide qualitative insight into the structure, integrity, and stability of the coating types, as well as their interaction with the steel substrate throughout the thermal treatment sequence and their compatibility with established SOC stack-assembly procedures.

The analyses were performed on single-side coated Crofer22APU coupons of 25 mm × 25 mm. Samples were investigated in the as-coated state, after the two reduction treatments (R1 and R2), and after the subsequent oxidation steps (S0, S1, and S2). In the XRD analysis, the starting powders were additionally included as reference. Surface measurements were conducted on a D4 Endeavour diffractometer (manufacturer: Bruker AXS, Karlsruhe, Germany) equipped with a 1D LynxEye detector. Monochromatic Cu Kα radiation was applied over a 2θ range from 10° to 80°, with a step size of 0.02° and a counting time of 0.75 s per step. All measurements were performed at room temperature.

Microstructural analysis was carried out on metallographic cross-sections to evaluate the continuity, density, and overall quality of the coatings, as well as their elemental distribution. Samples were embedded in epoxy resin, followed by automated multi-step grinding and polishing. Imaging was performed analogously to powder characterization using a GeminiSEM 450 and an Ultra 55 microscope (manufacturer: Zeiss, Oberkochen, Germany) with SE and BSE detection to visualize structural features and phase variations, respectively. Complementary EDS analysis was applied to characterize elemental distributions across the relevant processing states.

Chromium evaporation.—A key metric for evaluating the protective performance of interconnect coatings is the quantification of chromium evaporation under SOC-relevant conditions. Therefore, the coatings were exposed to the defined thermal treatment profile—comprising the simulated stack assembly procedure with a multi-step heating ramp, followed by 400 h of simulated SOC operation at 800 °C—to determine the cumulative release of volatile chromium species.

The exposures with the six coating variants (three MCF-based and three CMN-based) were conducted using the established denuder technique in a tubular furnace under continuous gas flow. To replicate the oxidizing, cathode-side atmosphere in SOFC stacks, humidified air containing 3% H_2O was employed. A porous SiC flow restrictor was mounted upstream of the samples to homogenize the gas distribution and minimize natural convection and backflow. The total flow rate was set to 6000 sml min^{-1}, ensuring a flow-independent regime inside the reactor. Coupons were placed on an alumina holder aligned with the direction of the flow.

At least three coupons of each type were subjected to each exposure, using a single-zone furnace for the continuous runs. Chromium evaporation was measured in situ according to the denuder method originally introduced by Froitzheim et al.[40] The vapor stream leaving the reactor passed through denuder tubes coated with Na_2CO_3, where volatile chromium species were trapped via the reaction shown in Eq. 1:

$$Na_2CO_3(s) + CrO_2(OH)_2(g) \rightarrow Na_2CrO_4(s) + CO_2(g) + H_2O \quad [1]$$

Denuder tubes were exchanged at regular intervals without interrupting the experiment. The removed tubes were leached with water, and the resulting solutions were analyzed using an Evolution 60S spectrometer (manufacturer: Thermo Scientific, Schwerte, Germany) to obtain the time-resolved chromium evaporation rates. Measurement points were defined after 100 h to represent stack assembly, and further after 200 h and 500 h to capture early operation stages.

For the chromium evaporation, mass gain, and ex situ ASR studies, specially designed samples were used to minimize the influence of uncoated areas. More than 99.8% of the surface was coated by preparing perforated coupons (15 mm × 17 mm) within a larger supporting frame (approx. 5 cm × 10 cm). Each coupon was connected to the surrounding frame by two 1 mm bridges (cf SI 1). This configuration enabled reliable electrical contacting of every single specimen, allowing all ten coupons to be coated simultaneously under identical conditions. Thermal treatments were carried out with the coupons still embedded in the frame; the specimens were detached afterwards to minimize handling-related damage at the edges. For samples subjected to direct oxidation without a prior reduction step, an additional one-hour stabilization at 850 °C in air was introduced to secure sufficient layer adhesion before detaching and exposure.

Mass gain.—Mass gain is a commonly used indicator of the oxidation kinetics of interconnect steels and the corrosion protection

provided by different coating types. In this study, the cumulative mass increase and corresponding mass gain rates were determined during the exposures.

In contrast to the chromium evaporation tests, the determination of mass gain was performed as a discontinuous process. The same equipment was employed as for the Cr evaporation study and several samples were exposed simultaneously, while specimens were removed at defined time intervals. For each data point, a minimum of three samples per coating type were temporarily taken out. Each removal step required cooling the samples to room temperature, followed by weighing, and subsequent reheating to the operating temperature.

The mass gain was calculated from the difference in sample weights recorded at the respective intervals. To isolate the contribution of steel oxidation beneath the coatings—i.e., the growth of the Cr_2O_3/$(Mn,Cr)_3O_4$ oxide scale by oxygen incorporation—the data were corrected by subtracting the previously quantified mass of volatilized chromium species. The resulting value is referred to as the "corrected mass gain" and is further evaluated in the results section on chromium retention capability.

For the pre-reduced samples, an additional contribution to the mass gain arises from the re-oxidation of the coatings back into the spinel phase. This contribution was calculated based on the stoichiometry of the reaction and the expected coating mass, and was included as a separate correction (details in the corresponding results section).

Area-specific resistance.—A critical aspect for assessing the suitability of interconnect coatings for stack operation is the area-specific resistance (ASR) of coated steel substrates under SOC-relevant conditions. Samples of the six coating types were measured in atmospheric air at 800 °C. The specimens used had previously undergone the 500 h exposure (i.e., the simulated stack joining and start-up phase).

Because the steel sheets used in the study were coated on both sides, whereas in real stack operation protection is applied only on the air-side, the evaluated ASR values were normalized to the contacted area and corrected by a factor of 0.5.

Measurements were performed in a tube furnace with contact to platinum wires and platinum meshes. Prior to measurement, both sides of each sample were sputtered with a thin gold layer, using a sputter coater, with a mask defining a 10 × 10 mm^2 area. After sputtering, gold paste (M-9875, manufacturer: METALOR Technologies, Marin, Switzerland) was applied to the sputtered region. After drying, the contact layer was solidified by sintering at 800 °C for 1 h. The resistance was measured after stabilizing the temperature in the furnace at 800 °C for 30 min, using a 4-wire, 2-point configuration. A Keithley source-meter unit of type 2400 (manufacturer: Keithley Instruments, Solon, Ohio, USA) was used for the measurements, with the applied current density set to 100 mA cm^{-2}. Eight resistance readings were taken every 8 min and averaged. A more detailed description of the ASR measurement technique is provided elsewhere.[41]

Glass sealant compatibility.—To evaluate the feasibility of directly applying the glass sealant onto the coating—thereby enabling full-surface coating of the interconnects without the need for masking—small-scale compatibility tests were conducted. These tests aimed to provide insight into the chemical and thermo-mechanical stability of the glass-coating interface, with particular emphasis on potential stresses arising from differences in thermal expansion due to phase precipitation. In addition, the experiments were designed to assess possible interdiffusion effects, which could impair the electrical insulation function of the glass sealant and thereby risk short-circuits within the stack. These investigations were carried out on basis of chemical compositions only and could be extended to electrical measurements in case of critical component formation.

For the joining procedure, a composite sealant based on a Ca-Ba-silicate glass with YSZ fibers as filler material, established at Forschungszentrum Jülich for SOC stack sealing applications, was employed in the form of screen-printed green foils. Details on the composition and development of this sealant and its application technique can be found elsewhere.[42,43] Circular blanks of 18 mm diameter were punched from the green foils and applied to the coated side of 25 mm × 25 mm Crofer22H coupons. Each sample was counter-faced with an uncoated Crofer22H coupon of identical dimensions. The gap thickness was defined by pre-sintered YSZ spacers with a thickness of 150 μm. Joining was performed following the multi-step procedure described in the experimental section on thermal treatments, under air atmosphere and with a joining load of 200 g.

A representative selection of coated specimen types was included in these tests, chosen based on the findings of the preceding investigations. The joined assemblies were evaluated by preparing cross-sections, analogous to the procedure used for single coupons. Subsequent characterization comprised SEM imaging and EDS analysis, including line scans across representative regions of the interaction zone at the center of the joint. Imaging was carried out using a Gemini 1 Sigma 300 VP scanning electron microscope (manufacturer: Zeiss, Oberkochen, Germany).

Flow-field structures.—Representative cut-outs of 25 mm × 25 mm from the flow fields of two interconnect types (F10 and CS^V) were prepared. These samples were integrated into the deposition setup in the same manner as flat substrates, with the electrode spacing adjusted to match the mid-height of the structures. Photographs of the two interconnect types and representative cut-outs are shown in the Supplementary Information (cf SI 2).

The investigations focused on the coating variant identified in the preceding studies as the most suitable candidate. Characterization followed the same procedures as for flat substrates, employing SEM imaging of embedded cross-sections (see in the characterization section on the evolution of phases and microstructures). Stitched overview images were generated from multiple micrographs, and additional detailed views were recorded in characteristic structural areas for direct comparison.

Results

Powder properties.—The powders exhibited highly comparable characteristics after identical mechanical processing, with very similar specific surface areas and d50 values—both identified as key parameters for the deposition behavior. This strong similarity in the powder properties allowed for an analogous processing route in the subsequent EPD steps. Representative PSD curves and SEM images are shown in Fig. 2, and key properties of both powders are summarized in Table II.

Microstructures and phases.—The characterization of microstructures along the specific steps of the thermal treatment sequence, as well as the associated phase evolution, was performed to qualitatively assess the integrity and structural condition of the coatings and to gain an understanding of the underlying transformations. A comparison of XRD surface analyses and SEM cross-sectional imaging for the group of MCF coatings is presented in Figs. 3a–3g), respectively.

The diffractograms at first confirmed the presence of the spinel phase after deposition, while additional Fe peaks were attributed to the signal of the underlying steel substrate due to the limited thickness of the non-densified EPD coating. For both reduction treatments (R1 and R2), the presence of Mn in its simple oxide form (MnO) and the occurrence of Co and Fe in metallic states were identified. Following the oxidizing heat treatment simulating the stack assembly, the original spinel phase was restored for all three programs (S0, S1, and S2), regardless of the preceding thermal history.

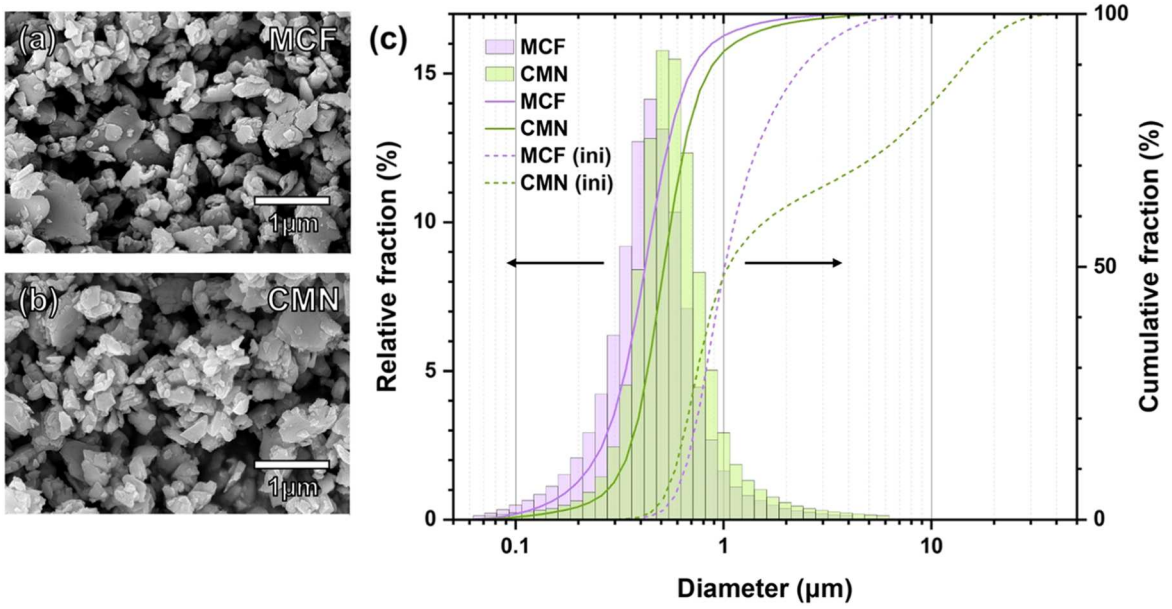

Figure 2. SEM-SE images of MCF (a) and CMN (b) powders after mechanical treatment, and particle size distribution of milled powders with untreated powders as reference (c).

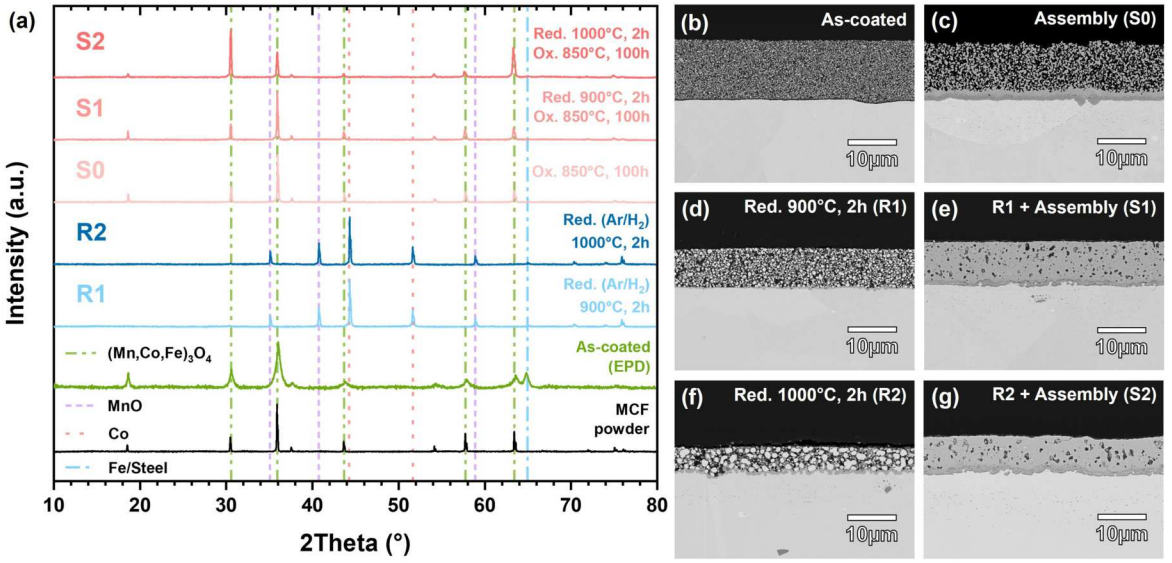

Figure 3. XRD (a) and cross-sectional SEM-BSE images (b)–(g) of MCF-EPD coatings in the specific states: as-coated (b), after the reduction steps R1 and R2 (d) and (f), and after the according (re-)oxidation steps (c), (e) and (g). The diffractograms include max. the five most significant peaks of each phase. The results indicate the partial reduction of the spinel to metal particles (Co + Fe) and a MnO matrix, accompanied by re-oxidation induced densification.

Table II. Powder characteristics of MCF and CMN powder as prepared for this study; Values for d10, d50 and d90, as well as mass-specific surface area.

Composition	Abbreviation	d10 (µm)	d50 (µm)	d90 (µm)	SSA (m^2g^{-1})
$MnCo_{1.9}Fe_{0.1}O_4$	MCF	0.23	0.42	0.73	12.39
$CuMn_{1.8}Ni_{0.2}O_4$	CMN	0.32	0.52	0.89	10.39

Cross-sectional analysis revealed coherent, intact coatings in all investigated stages without the formation of cracks or comparable defects. For the direct oxidizing sintering route, a slight reduction in coating thickness accompanied by residual open porosity was observed. At the same time, the development of a distinct chromium oxide scale exceeding 1 µm in thickness became visible, with only the directly adjacent region of the MCF coating of comparable thickness appearing consistently dense (cf Figs. 3b and 3c).

In the reduced states, a pronounced decrease in coating thickness was observed, with R2 showing particularly strong shrinkage to less than half of the initial thickness and a correspondingly reduced porosity. The multiphase nature of these states, as indicated by the XRD analysis, was also evident in the cross-sections (cf Figs. 3d and 3f). Additional insight into the distribution of phases and elements across the different stages was provided by detailed EDS mappings (for both MCF and CMN), exemplified for the two-step treatment R2/S2 in Fig. 5. These results indicated that the metallic phase was embedded as spherical particles within an MnO matrix, with R2 showing substantially larger metallic particles than R1. After the final oxidizing step, the previously reduced samples exhibited an increase in coating thickness compared to their respective reduced

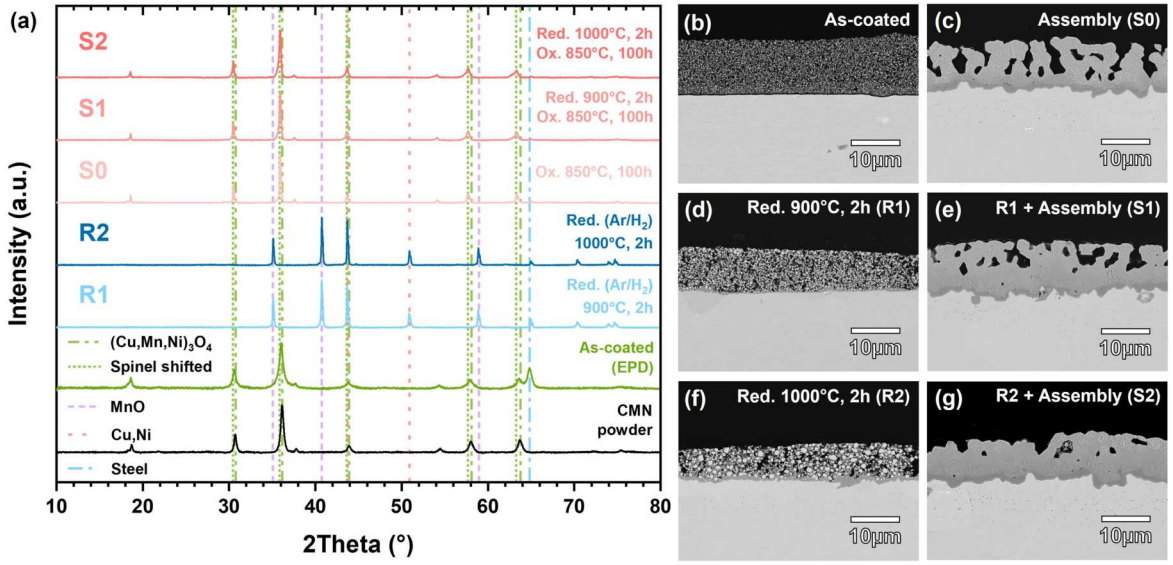

Figure 4. XRD (a) and cross-sectional SEM-BSE images (b)–(g) of CMN-EPD coatings in the specific states: as-coated (b), after the reduction steps R1 and R2 (d) and (f), and after the according (re-)oxidation steps (c), (e) and (g). The diffractograms include max. the five most significant peaks of each phase. The results indicate the partial reduction of the spinel to metal particles (Cu + Ni) and a MnO matrix, accompanied by re-oxidation induced densification.

states, though the overall thickness in the final state remained lower for R2 compared to the other programs. Both two-step treatments resulted in closed porosity, with S2 showing fewer but slightly enlarged pores compared to S1 (cf Figs. 3e and 3g).

For the group of CMN coatings, an analogous comparison of XRD surface analyses and SEM cross-sections is presented in Figs. 4a–4g), respectively.

Comparable to the analyses of the MCF coatings, the CMN samples exhibited similar general tendencies, but with several decisive differences. The diffractograms confirmed the presence of the spinel phase after deposition, with an additional Fe peak again attributed to the steel substrate due to the low coating thickness. After reduction (R1 and R2), the diffraction patterns indicated the presence of metallic Cu and Ni phases alongside MnO. Following the oxidizing treatments, all three sample types were re-converted into the original spinel structure. However, in contrast to MCF, all three oxidized CMN coatings showed a systematic shift of the characteristic spinel peaks towards lower 2θ angles, suggesting a slight compositional change relative to the initial state.

Cross-sectional analysis further demonstrated that the identical processing route for both spinel powders, covering powder preparation and deposition, enabled the fabrication of similarly uniform green layers. CMN coatings in the as-deposited state appeared continuous and free of visible defects, with thicknesses in the range of 10–15 µm (cf Fig. 4b). After direct oxidizing treatment, the coatings retained a porous morphology with pore channels partially extending through the entire thickness (cf Fig. 4c). Compared to the analogous MCF coatings, the CMN samples exhibited a noticeably coarser microstructure combined with a slightly more pronounced thickness reduction.

After both reduction programs, the CMN coatings again showed pronounced shrinkage, accompanied by the formation of spherical metallic Cu and Ni particles embedded within a MnO matrix. In R2, the metallic features appeared distinctly coarser compared to R1, combined with the occurrence of isolated large pores in some instances spanning major parts of the coating thickness (cf Figs. 4d and 4f). After the simulated stack assembly, the pre-reduced coatings displayed a reduced thickness compared to the as-deposited state, but with re-thickening relative to the reduced condition (cf Figs. 4e and 4g). The strongest shrinkage with the lowest residual porosity was again associated with protocol S2. Nevertheless, in comparison to MCF, the residual porosity in CMN exhibited a different morphology, with a particularly surface-accessible distribution combined with a continuous, dense base layer of several micrometers adjacent to the substrate. Complementary SEM surface images of all types can be found in the Supplementary Information (cf SI 3).

The formation of a chromia scale was detected for all CMN specimens, though the steel-coating interface appeared less regular than for MCF. EDS mappings highlighted the pronounced difference in chromium distribution between the two spinel types after simulated joining (Figs. 5c and 5d for R2/S2). For MCF, chromium was clearly confined to the chromia scale at the steel-coating interface. In contrast, CMN exhibited a far-reaching chromium penetration, extending into surface-accessible porosity and accompanied by a concurrent depletion of the spinel phase, most evident in the Ni and Cu signals.

Trace levels of zirconium, as impurities in the commercial powder, were also detected in the MCF coatings, visible in the corresponding mappings.

Chromium retention capability.—The spectrometrically evaluated chromium evaporation data, collected continuously during exposure, are summarized for the six investigated coating types with measurement points at 100 h (simulated assembly) and at 200 h and 500 h (simulated stack start). As a reference for uncoated Crofer22APU steel, data from a study by Reddy et al.[44] were included. Although the referenced study employed a constant exposure at 800 °C, while the present work involves an initial 100 h joining step at 850 °C, the comparable measurement methodology and identical denuder set-up provide a suitable basis for comparison. Moreover, the slightly milder conditions in the reference study ensure that no artificial improvement of the present results is implied.

The chromium release rates of the six coating types, compared with the uncoated reference, are presented in Fig. 6a, while Fig. 6b shows the isolated data set for the MCF coatings. Across all exposure conditions, the application of protective coatings resulted in a substantial reduction of chromium volatilization. However, two distinct groups emerged, separated by coating composition. The MCF coatings consistently reduced chromium evaporation by a factor of 10–20 compared to CMN and by approximately a factor of 30 compared to the uncoated steel. Within both groups, the two-step treatment including pre-reduction at 1000 °C (S2) provided the lowest evaporation rate. For MCF, the other two treatments (S1 and S0) yielded slightly higher cumulative release, but remained

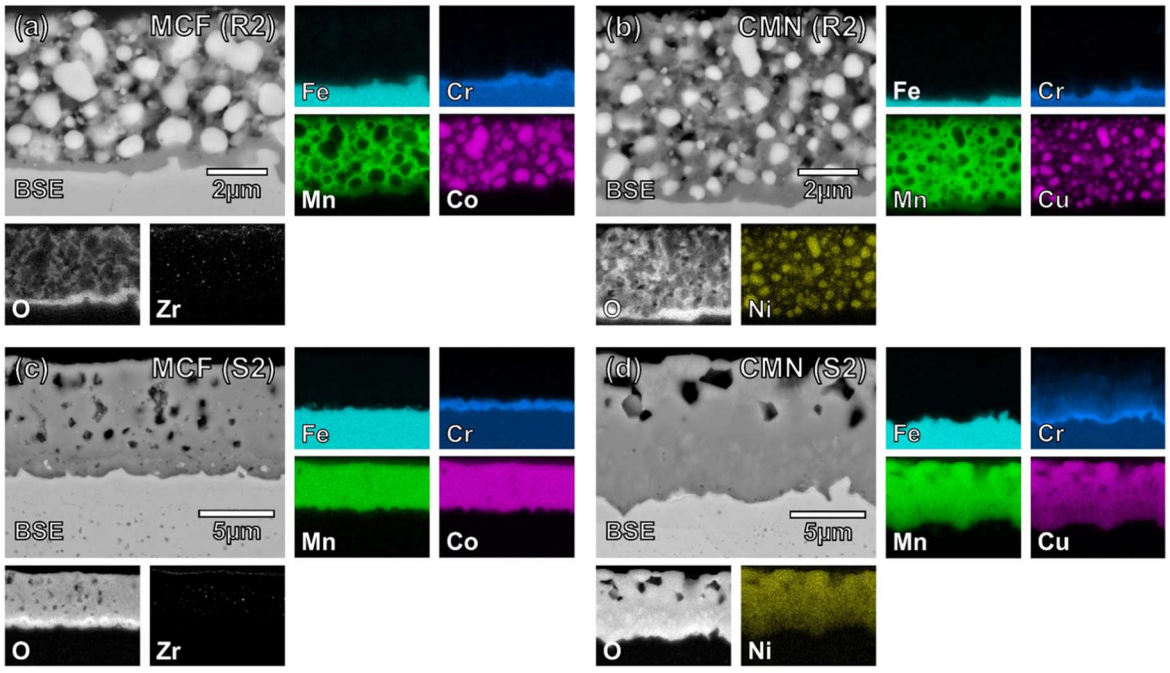

Figure 5. Cross-sectional EDS mappings of MCF and CMN coatings after R2 treatment (2 h reduction at 1000 °C) (a), (b) and after the subsequent oxidation (100 h oxidation at 850 °C) accounting to the overall treatment S2 (c), (d). The elemental analyses reveal a pronounced localization of Cr within the chromia scale for the MCF coating, whereas the Cu-Mn spinel shows extensive Cr spreading throughout the coating.

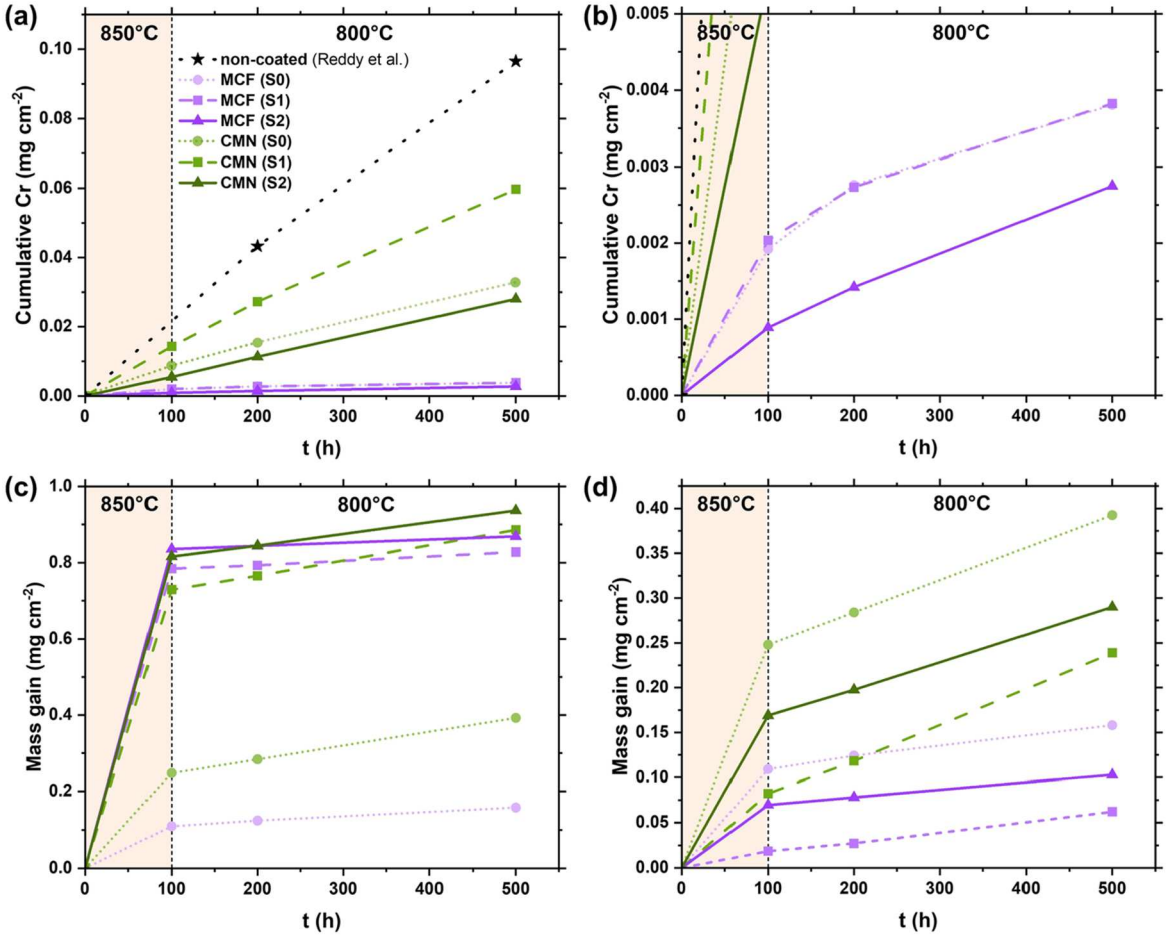

Figure 6. (a) Cumulative Cr evaporation curves for all coating types and (b) in detail for MCF samples, as well as corrected mass gains of EPD-coated and non-coated Crofer22APU substrates (reference): (c) after correction for Cr evaporation and (d) after further subtraction of the re-oxidation contribution of the spinel coating.

close to each other. In contrast, for CMN the 900 °C pre-reduction route (S1) deviated towards significantly higher values.

Oxidation protection.—The mass gains of the six coating types were determined discontinuously by repeated removal, weighing, and reinsertion of the samples during the 500 h exposure. Analogous to the chromium evaporation data, the results were processed and plotted, as shown in Fig. 6c.

From the phase analyses it is evident that during the assembly step, coatings subjected to pre-reduction undergo a complete re-oxidation to the spinel phase. This transformation is necessarily associated with a mass increase due to oxygen incorporation into the coating. The contributions of this re-oxidation to the total mass gain are governed by the spinel stoichiometry and therefore differ between the two compositions, as outlined by the following reactions (Eqs. 2 and 3):

$$1.0\ MnO + 1.9\ Co + 0.1\ Fe + 1.5\ O_2 \rightarrow 1\ MnCo_{1.9}Fe_{0.1}O_4 \quad [2]$$

$$1.8\ MnO + 1.0\ Cu + 0.2\ Ni + 1.1\ O_2 \rightarrow 1\ CuMn_{1.8}Ni_{0.2}O_4 \quad [3]$$

Based on these stoichiometries, the expected re-oxidation-induced mass increases relative to the reduced state amount to +25.5% for MCF and +23.3% for CMN. Combined with the determined average coating masses, these contributions formed the basis for the applied corrections to the measured mass gain curves. The doubly corrected data are presented in Fig. 6d, while the Supplementary Information (cf SI 4) additionally provides the uncorrected curves as well as curves corrected only by subtracting the 100 h value, in order to fully exclude the oxidation effects during the assembly phase.

The plots in Figs. 6c and 6d show a continuous increase in mass gain relative to the initial state for all coated samples, with a pronounced flattening of the curves after the first 100 h. When the calculated re-oxidation contributions for the S1 and S2 types are subtracted, this effect is substantially reduced, and the overall trends during the exposure duration reflect the same separation already observed in the chromium evaporation results: the group of MCF coatings consistently exhibits lower mass gain compared to the CMN group. Particularly after the simulated assembly step, the MCF coatings show systematically lower increases in the mass gain curves. Within both groups, MCF and CMN, the lowest mass gain rates during continued exposure after assembly are observed for the S2 samples, i.e., after pre-reduction at 1000 °C.

During the exposure period following the initial 100 h, a decrease in the slope of the cumulative mass gain is evident for all coated sample types. When including the first 100 h, however, the picture becomes less clear. It should be noted again that correction of the re-oxidation contributions relies on an average coating mass. Deviations in the actual coating mass of individual samples could therefore significantly affect the accuracy of the calculated contribution, although it is not possible to quantify the error or provide an error range.

Electrical properties.—The area-specific resistances, measured ex situ after 500 h total exposure time including simulated stack assembly and the first 400 h of stack operation, are compared in Fig. 7a.

The measurements showed values consistently around or below 20 mΩ cm^2, with a slight tendency of the CMN-coated samples towards lower values. Only the CMN-S1 type deviated from this trend, displaying an increased ASR of about 25 mΩ cm^2, in line with the observations from the preceding exposure-related investigations.

While the variation between individual measurements of a given sample was minimal, the uncertainties related to possible differences in the contact configuration (e.g. caused by the manual application of the Au paste) are assumed to be more significant. Therefore, a precise differentiation within the investigated sample groups is not meaningful, whereas comparisons with literature data and general expectations remain more relevant.

Glass sealant interaction.—The interaction of glass sealant with the spinel coatings was evaluated based on cross-sectional SEM imaging and EDS analyses, exemplarily for MCF and CMN coatings processed via protocol R2/S2, i.e., coatings reduced at 1000 °C prior to sealing. Comparative micrographs with line scans at representative positions in the center of the joining zone are shown in Fig. 7b for MCF and Fig. 7c for CMN.

Cross-sections revealed extensive infiltration of the glass sealant into both coating types. In both cases, largely dense composite layers formed, with only localized residual porosity remaining in the MCF sample. Moreover, the microstructure of the MCF coating resembled the morphology obtained under free sintering, with a comparable thickness.

In contrast, the CMN coating exhibited a pronounced alteration in both microstructure and thickness compared to its reference state after air sintering without contact to the glass. A significant reduction in coating thickness by approximately 50% was observed, and the resulting composite was characterized by a largely displaced coating core with only a remaining bottom and top layer enclosing infiltrated glass. In both cases, the bonding between the glass and the EPD coatings occurred coherently, without evidence of delamination, cracking, or related defects.

Line scans confirmed the infiltration of glass components into the MCF coating, with elements such as Si, Ca, Ba, and Zn detected within the layer. The infiltrated zone did not show the typical crystallization of the glass matrix and maintained amorphous with precipitates formed within the coating, while typical feldspathoid reinforcement fibers, here indicated by Al, were only present outside the coating. For the CMN sample, similar infiltration of glass constituents into the former coating zone was observed. However, at the same time, the principal spinel components showed a markedly different behavior: their presence within the original coating was diminished, and redistribution into the glass sealant was evident. In particular, Cu no longer showed a clear localization near the steel substrate but was instead dissolved and irregularly precipitated throughout the glass matrix. For MCF, only a minor diffusion of Co into the adjacent glass phase was detectable. Further support for these findings is provided by larger-area analyses (EDS mappings), which are available in the Supplementary Information (cf SI 5).

A further distinction between the two coating systems concerned the localization of Cr. For the MCF sample, a coherent Cr-rich oxide layer adjacent to the steel substrate was present, similar to that observed under other thermal treatments, with only a weak Cr enrichment near the outer surface of the coating. In the CMN case, an additional continuous Cr-rich layer formed above the remnants of the former EPD coating, accompanied by a pronounced Mn signal, while the oxide layer at the substrate remained comparable in morphology.

Relevant flow-field structures.—Based on the preceding results, the coating material MCF in combination with the S2 thermal treatment protocol (i.e., the two-step route with pre-reduction at 1000 °C) was selected for further evaluation regarding its adaptability to real interconnect structures. Cross-sections of the two prepared substrate types with MCF coatings after heat treatment are shown in Fig. 8 (F10-type interconnect with rib-channel design) and Fig. 9 (CS^V-type interconnect with corrugated design). Characteristic zones of each geometry were analyzed in detail and are displayed at two different magnifications.

For both substrate types, the coatings exhibited continuous and coherent layers throughout all regions without evidence of defects such as cracks or delamination. Across both geometries, variations in coating thickness were observed depending on the specific position within the structural unit. In the rib-channel and corrugated structures, increased coating thicknesses were detected on the ridges (cf Figs. 8c and 9c), which gradually decreased along the flanks (cf Figs. 8b and 9b) and reached their lowest values in the valleys (cf Figs. 8d and 9d). The variation in thickness spanned a factor of two or more. Notably, even in areas characterized by pronounced

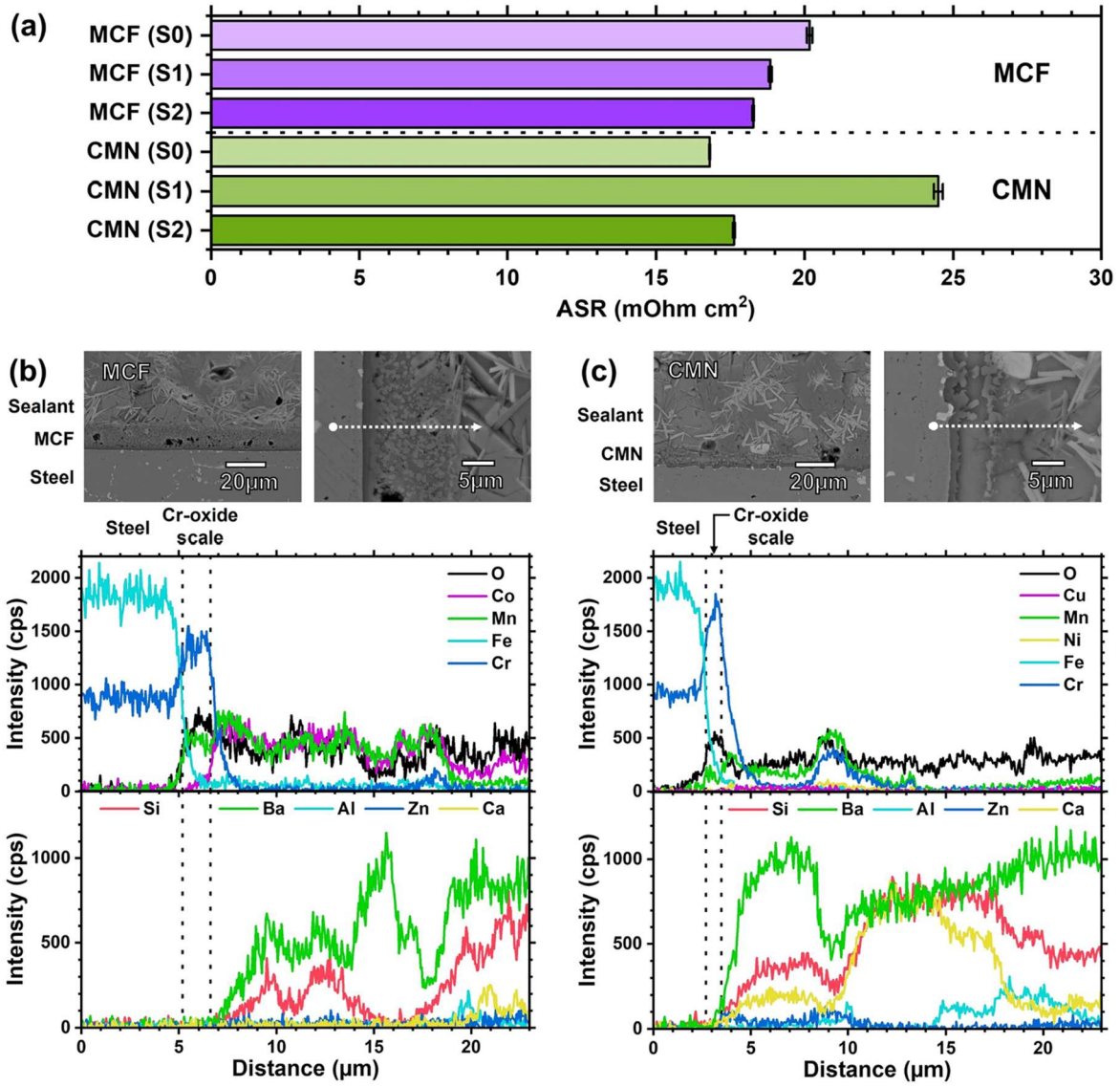

Figure 7. (a) Ex-situ ASR values measured after 500 h of exposure. (b), (c) SEM-BSE images and corresponding EDS line scans of glass sealant-coating composites: glass sealant applied to MCF (b) and CMN (c) coatings after R2 reduction treatment, followed by crystallization for 100 h at 850 °C in air.

differences in surface-to-volume ratio and complex stress states during thermal treatment—particularly the convex and concave zones of the F10 structure (cf Figs. 8e and 8f)—the coatings remained continuous and coherent, without the formation of defects.

The overall coating thicknesses on the structured substrates ranged slightly below and above those obtained on flat substrates. The microstructures closely resembled those of flat samples, with a general tendency towards increased layer thickness. In all regions of the structured substrates, the coatings displayed the characteristic closed porosity typical of the two-step S2 treatment on flat coupons.

Discussion

Structural implications of thermal treatments.—The structural investigations on flat Crofer22APU substrates demonstrate that the developed EPD process enables the fabrication of uniform and coherent coatings for both selected spinel compositions. The differences in the microstructural evolution during thermal treatments within one material system are attributable to variations in sintering activity depending on the pre-treatment. The overall low shrinkage, as well as the marginal particle coalescence with remaining open porosity observed for MCF after direct oxidation (S0), results from its limited sinterability of the loosely bound powder compact after deposition. The concurrent growth of a chromia scale below the thin, continuous bottom part of the coating is explained by the strongly facilitated inward migration of oxygen through the open porosity during the simulated assembly step. While the spinel phase remains stable, the microstructure of MCF-S0—with its open porosity—already compromises the protective function in terms of both corrosion resistance and chromium retention.

For CMN coatings exposed only to the assembly step, the stronger redistribution of material compared to MCF reflects the effect of Cu on the sinterability of Mn-based spinels and the overall higher sintering activity of Cu-Mn spinels.[21,22,45,46] Nevertheless, the formation of a porous structure with pore channels spanning the entire coating thickness is again a direct consequence of the low initial density of the EPD coatings. This microstructure does not provide favorable conditions for blocking inward oxygen migration or volatile chromia release. The systematic shift of the spinel peaks observed in the phase analysis likely originates from the incorporation of chromium into the spinel lattice, resulting in the formation of a partially substituted $(Cu,Mn,Ni,Cr)_3O_4$ spinel.

The shrinkage detected for both MCF and CMN during reduction is clearly linked to oxygen release and the enhanced diffusivity of the

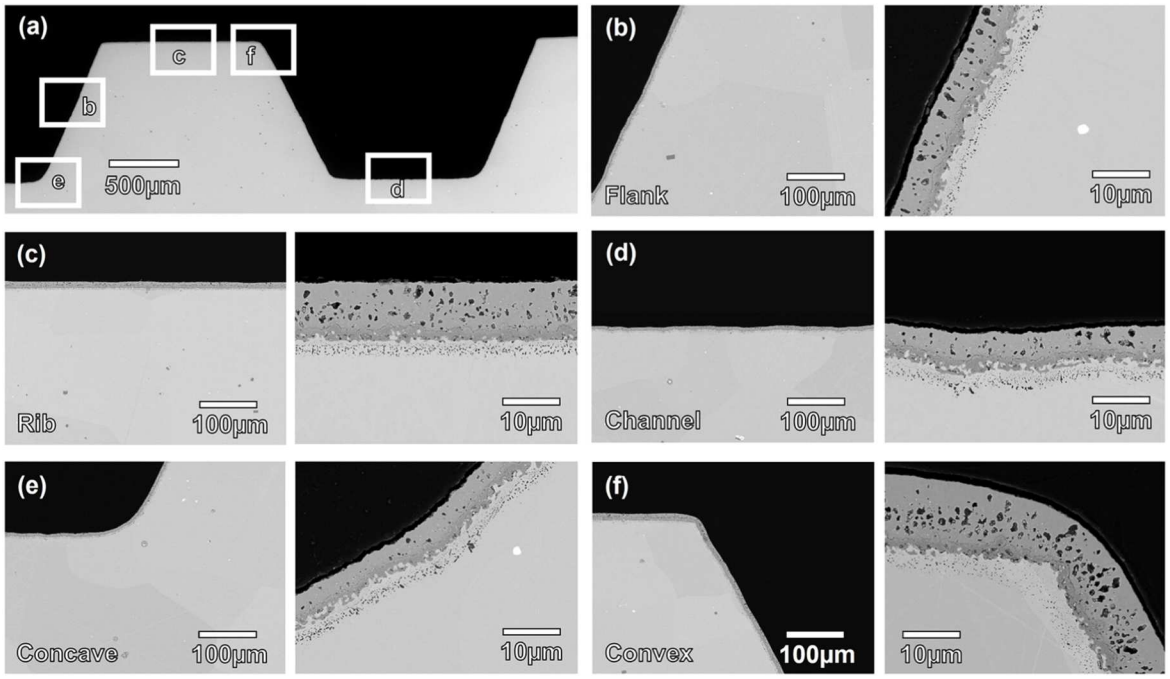

Figure 8. MCF-EPD coating on rib-channel-type flow-field structure, cut out of F10 interconnect, heat-treated with two-step protocol S2. Stitched overview (a), and detailed SEM-BSE images in characteristic areas along the structural unit (b)–(f).

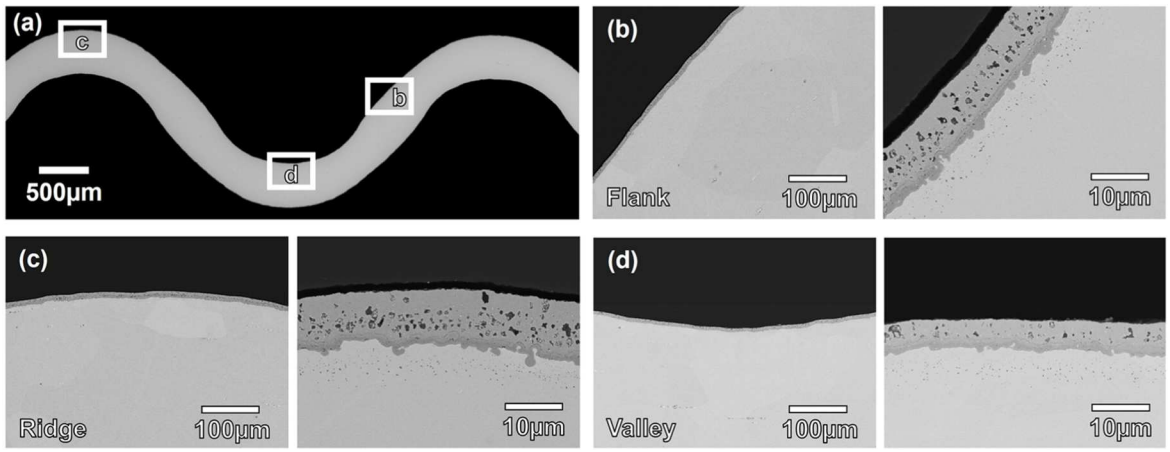

Figure 9. MCF-EPD coating on wave-type flow-field structure, cut out of CS-type interconnect, heat-treated with two-step protocol S2. Stitched overview (a), and detailed SEM-BSE images in characteristic areas along the structural unit (b)–(d).

metallic phases formed. The accompanying reduction in pore fraction, more pronounced at the higher reduction temperature (R2 compared to R1), is attributed to this mechanism, as is the agglomeration of metallic particles, driven by temperature-enhanced diffusion. The incomplete transformation into metallic phases and MnO is consistent with the limited reducing potential of the chosen conditions, by means of remaining O_2 partial pressure and H_2 concentrations of a few vol.%, and aligns with reports on reactive sintering and partial reduction in similar systems.[31,36,47]

After re-oxidation, MCF coatings form uniform layers with closed porosity, attributable to the homogeneous re-incorporation of oxygen into an already densified structure. The slightly higher degree of densification in the S2 protocol stems from the more compact microstructure resulting from the preceding high-temperature reduction. As a result, MCF coatings subjected to the two-step thermal treatments exhibit a property profile that is more favorable.

In contrast, the CMN coatings treated with the same two-step protocols developed a coarser and more irregular microstructure, with a noticeably weaker densification compared to the analogous MCF coatings, particularly for the S1 protocol. The reduced contribution of re-oxidation to densification in CMN relative to MCF is related to the higher Mn content of the base spinel ($CuMn_2O_4$ vs $MnCo_2O_4$; cf Eqs. 2 and 3). Combined with the intrinsic tendency of Cu-Mn spinels towards particle agglomeration, this results in coarse microstructures after re-oxidation, consistent with the grain coarsening also observed after direct oxidation of CMN.

The consistent shift of spinel peaks to lower 2θ values in CMN coatings after the assembly step, in combination with EDX analysis, independent of the pre-treatment, supports the conclusion of chromium incorporation into the spinel structure (cf Fig. 5d). This points to accelerated diffusion processes and reflects the known tendency of Cu-Mn spinels to permit chromium transport and trapping.[23,44,48] Such behavior already raises fundamental concerns regarding the protective effectiveness of CMN-based coatings over long-term operation.

The irregular interface observed between CMN coatings and the steel substrate is also likely a result of the strong sintering activity of

the spinel and its interaction with steel components, particularly chromium. This is critical in terms of thermo-mechanical stability.

Taken together, the structural analysis across the selected thermal treatments and the integration of the assembly step highlight the superior suitability of the established MCF composition and the benefits of two-step thermal treatments. For CMN, by contrast, the results raise the question of whether coatings of this composition—or Cu-Mn spinels more generally—can be integrated into existing thermal processes such as the 100 h assembly step, or whether lower joining temperatures and/or shorter dwell times are essential to avoid significant degradation during assembly itself and to achieve beneficial microstructural properties.

Protective performance under simulated stack conditions.—The exposure experiments under simulated stack conditions have reinforced the tendencies already indicated by the structural analyses. The markedly better chromium retention of the MCF coatings compared to the CMN coatings—partially only providing minor improvements over the uncoated reference—underlines the excellent protectivity of MCF against chromium poisoning of the air electrode. The visible flattening of the Cr evaporation can be attributed to the slightly elevated temperatures and microstructural evolution during the simulated stack-assembly phase.[44,49]

The distinctly lower chromium release measured for the MCF samples subjected to pre-reduction at 1000 °C (R2) can likely be linked to the slightly higher densification, in particular the formation of a denser and more continuous top layer (cf SI 3). The nearly identical behavior of the S0 and S1 types suggests that residual open porosity remains in these coatings, facilitating the outward diffusion of volatile chromium species. Nevertheless, the absolute chromium evaporation rates of all MCF coatings are on a very low level, in line with favorable values reported in the literature.[44,49] In contrast, the substantially poorer chromium retention of the CMN-coated substrates is consistent with the chromium penetration observed after stack-assembly in the microstructural analysis. The nearly identical results of CMN-S0 and CMN-S2, together with only a marginal advantage of the two-step treatment, indicate that the limited chromium retention of CMN under the present conditions is dominated by intrinsic material properties rather than by the specific microstructure formed. The disproportionately poor performance of CMN-S1, however, likely points to quality issues in this specimen group. Since all coupons were coated in one batch and cut from the same carrier plate, the occurrence of critical defects such as cracks due to unnoticed process deviations cannot be excluded. Based on the structural results, the degradation of CMN-S1 cannot be sufficiently explained by microstructural arguments alone.

For the oxidation-related mass gains, the separation of the pre-reduced specimens (S1 and S2) that is visible in the chromium-corrected curves is attributable to the re-oxidation of the coatings. After applying the second correction, accounting for both chromium evaporation and the calculated mass gain from re-oxidation, the trends converge with the findings from the evaporation tests: the MCF group over the duration of the exposure exhibits lower mass-gain rates than the CMN group, while the uncoated reference shows the highest values. This confirms the superior protectivity of MCF.

For both spinels, the lowest mass-gain rates after the first 100 h of exposure are observed for the R2 condition. In MCF this can again be attributed to the denser top layer (cf SI 3), which strongly slows the inward migration of oxygen. In CMN, the effect may be caused by the combined action of a slightly denser top layer (cf SI 3) and the comparatively thick and continuous bottom layer adjacent to the substrate.

The robustness of the double-corrected curves must, however, be considered with caution. Small variations in the actual coating mass can introduce errors into the re-oxidation correction, which is based on averaged values. This mainly affects the interpretation within the assembly phase, while the longer-term trends during subsequent operation remain unaffected and still provide a reliable picture (cf SI 4).

It must further be noted that the processes occurring during the one-hour fixation treatment of the samples exposed in air solely were not included in the data. This introduces a minor underestimation of mass gain and chromium release, but does not affect the overall trends.

In terms of electrical performance, the coatings exhibit area-specific resistance values around or below 20 $m\Omega\ cm^2$ after 500 h, which is fully acceptable for stack operation. With respect to the aim of maintaining interconnect-related ASR contributions well below 100 $m\Omega\ cm^2$, all coating types clearly remain within the target range even after exposure to harsh joining conditions and several hundred hours at 800 °C. Only the CMN-S1 samples show slightly elevated values, consistent with their inferior performance in the complementary degradation metrics. Interestingly, the generally stronger degradation observed for CMN in terms of oxidation is not reflected in uniformly higher ASR values. This may result only to a minor extent from the intrinsically higher electrical conductivity of CMN compared to MCF, and more likely from improved contacting effects, for instance due to the larger interfacial area between the Au contact layer and the porous CMN coatings. Such effects could partly compensate for degradation-related losses.

Integration aspects: Sealing compatibility and flow-field adaptation.—From the integration perspective, the investigations on sealing compatibility and flow-field structures provide clear insights. The formation of a dense composite without the occurrence of defects such as cracks or delamination during direct joining indicates that the selected MCF and CMN coatings are thermo-mechanically feasible. However, the pronounced interaction observed within the CMN sample, including the expansive dissolution of the coating into the glass, represents a potentially severe issue under SOC operating conditions. While the present investigation cannot fully assess how the interfacial interaction might evolve over time or whether stress-induced defects could eventually lead to leakage, a major risk arises from the diffusion of metallic copper. The extensive Cu penetration, facilitated by its high reactivity and diffusivity and by the large active surface area of metallic Cu present at the onset of the joining process, could critically impair the electrical insulation of the glass sealant and may even cause short-circuiting during stack operation.

In contrast, the morphological stability of MCF coatings during joining, accompanied by the formation of a dense, continuous composite layer, is highly beneficial. The absence of significant diffusion of conductive species into the glass sealant suggests that reliable electrical insulation can be maintained. Nevertheless, further investigations of insulation performance, gas tightness, mechanical durability, and long-term coating-glass interactions remain essential before drawing definitive conclusions on stack-level applicability.

The transfer of the most promising coating candidate—MCF with the two-step heat treatment S2—onto real structures confirmed the general suitability of EPD for geometries relevant to SOC interconnects. Comparable performance is further expected for alternative designs based on sheet forming or bulk machining, including localized features such as dimples.

The results underline the advantages of EPD as a suspension-based, non-line-of-sight technique capable of producing continuous and homogeneous coatings across all characteristic zones of the structures. The excellent coating quality at sharp edges (cf Figs. 8e and 8f) and the absence of stress-induced cracking or delamination are particularly positive, as these regions are highly prone to mechanical stress during thermal cycling.[50]

The observed thickness variations along the profile are attributable to several factors. The reduced coating thicknesses in recessed zones are primarily related to the larger effective electrode distance and the locally lower surface-to-volume ratio, which in turn lead to weaker electric fields and local suspension depletion. This variation is not necessarily detrimental, provided that a continuous and sufficiently dense coating is maintained in all areas. Moreover, the preferential thickening at elevated features and sharp edges is advantageous, since these zones are in direct contact with the air electrode and thus demand the highest level of protection.

Overall, these findings confirm the suitability of EPD as a coating method and demonstrate the compatibility of the developed MCF

coatings with the applied thermal treatment for relevant interconnect structures. Considering the investigations of different thermal processing routes together with the performance indicators, this provides a robust foundation for transferring the approach to real stack components and for subsequent long-term testing under system-relevant conditions.

Conclusions

In this work, a comprehensive comparison of two spinel-type coating materials, $MnCo_{1.9}Fe_{0.1}O_4$ (MCF) and $CuMn_{1.8}Ni_{0.2}O_4$ (CMN), was carried out to evaluate their suitability as protective coatings for SOC interconnects. Electrophoretic deposition (EPD) proved to be a highly versatile and reliable processing route. It enabled a uniform deposition of both compositions after identical powder preparation, and moreover, demonstrated excellent applicability to complex interconnect geometries representative of real stack designs.

Particularly favorable performance was achieved when applying two-step thermal treatment protocols involving a pre-reduction step followed by re-oxidation. A reduction step at 1000 °C for 2 h was identified as especially beneficial, resulting in dense, coherent coatings with enhanced protective functionality under operating conditions. Importantly, the subsequent oxidation treatment was fully compatible with established stack fabrication and running-in procedures, thereby allowing integration into existing manufacturing routes without additional processing steps.

While this two-step treatment also improved the performance of the Co-free CMN composition, the overall comparison clearly confirmed the superior suitability of the established MCF material. MCF coatings provided significantly enhanced protection against chromium evaporation and steel substrate oxidation, while maintaining favorable electrical properties. CMN coatings, in contrast, showed weaker protective capability, particularly with respect to chromium retention, though their performance may remain promising for application in intermediate-temperature SOC systems.

Initial sealing tests indicated the feasibility of direct joining onto the coatings, with MCF in particular forming dense, stable composites without detrimental interactions. Together with the successful transfer of optimized coatings to interconnect flow-field structures, these results highlight the high potential of the developed EPD approach for implementation under application-relevant conditions.

Overall, this study establishes MCF-based coatings prepared by EPD and optimized through a two-step thermal treatment as a robust and process-compatible solution for SOC interconnects. By combining excellent chromium retention, oxidation protection, and electrical performance with proven adaptability to sealing and flow-field structures, the developed approach lays the groundwork for their direct implementation into existing stack designs.

Brief Summary

This study compares $MnCo_{1.9}Fe_{0.1}O_4$ (MCF) and $CuMn_{1.8}Ni_{0.2}O_4$ (CMN) coatings for SOC interconnects, deposited by electrophoretic deposition (EPD). Two-step thermal treatments with a reduction step prior to oxidation proved most effective, especially at 1000 °C. MCF coatings showed superior chromium retention, oxidation resistance, and microstructural stability compared to CMN. EPD enabled uniform coatings not only on flat coupons but also on complex flow-field structures. The results highlight MCF-EPD coatings as a process-compatible and scalable solution for SOC stacks.

Acknowledgments

The authors gratefully acknowledge the colleagues who contributed to this work through practical assistance and discussions, including: M. Xhonneux (IMD-2), A. Hilgers (IMD-2), V. Bader (IMD-2), Dr Y. J. Sohn (IMD-2).

The funding from the European Union's Horizon Europe research and innovation program under grant agreement N°101058784 is gratefully acknowledged. Additional thanks are extended to Marion Technologies for providing the spinel powder and to VDM Metals for providing Crofer material within the framework of the project NOUVEAU.

The authors acknowledge Forschungszentrum Jülich for supporting open-access publishing through its participation in Projekt DEAL.

Declaration of Generative AI and AI-Assisted Technologies in the Writing Process

During the preparation of this work the authors used ChatGPT (Version 5) by OpenAI in order to improve the language of the manuscript. After using this service, the authors reviewed and edited the content as needed and take full responsibility for the content of the publication.

ORCID

Martin Hilger https://orcid.org/0009-0003-2642-1444
Thorbjørn Krogsgaard https://orcid.org/0009-0003-4135-6775
Sonja-Michaela Groß-Barsnick https://orcid.org/0000-0003-4143-1571
Doris Sebold https://orcid.org/0000-0001-8595-8055
S. Shrikanth https://orcid.org/0000-0003-0517-2592
Jan Froitzheim https://orcid.org/0000-0001-6339-6004
Christian Lenser https://orcid.org/0000-0001-5636-2201
Norbert H. Menzler https://orcid.org/0000-0001-7091-0980

References

1. A. Hauch et al., "Recent advances in solid oxide cell technology for electrolysis." *Science*, **370**, eaba6118 (2020).
2. H. Liu, M. Yu, X. Tong, Q. Wang, and M. Chen, "High temperature solid oxide electrolysis for green hydrogen production." *Chem. Rev.*, **124**, 10509 (2024).
3. J. Li et al., "Advancements in solid oxide fuel cell technology: bridging performance gaps for enhanced environmental sustainability." *Adv Energy and Sustain Res*, **5**, 2400132 (2024).
4. E. D. Wachsman, D. Oh, E. Armstrong, D. W. Jung, and C. Kan, "Mechanistic understanding of Cr poisoning on $La_{0.6}Sr_{0.4}Co_{0.2}Fe_{0.8}O_{3-\delta}$ (LSCF)." *ECS Trans.*, **25**, 2871 (2009).
5. Q. Fang, N. H. Menzler, and L. Blum, "Degradation analysis of long-term solid oxide fuel cell stacks with respect to chromium poisoning in $La_{0.58}Sr_{0.4}Co_{0.2}Fe_{0.8}O_{3-\delta}$ and $La_{0.6}Sr_{0.4}CoO_{3-\delta}$ cathodes." *J. Electrochem. Soc.*, **168**, 104505 (2021).
6. T. Horita, "Chromium poisoning for prolonged lifetime of electrodes in solid oxide fuel cells - Review." *Ceram. Int.*, **47**, 7293 (2021).
7. Y. Hao, R. Zhu, H. Cao, Z. Liu, R. Ran, and G. Yang, "A mini-review on mitigating degradation of metallic interconnects in solid oxide cell stack systems: Advances, challenges, and solutions." *Energy Fuels*, **39**, 18751 (2025).
8. J. C. W. Mah, A. Muchtar, M. R. Somalu, and M. J. Ghazali, "Metallic interconnects for solid oxide fuel cell: a review on protective coating and deposition techniques." *Int. J. Hydrogen Energy*, **42**, 9219 (2017).
9. J. Mao et al., "Progress in metal corrosion mechanism and protective coating technology for interconnect and metal support of solid oxide cells." *Renew. Sustain. Energy Rev.*, **185**, 113597 (2023).
10. J. H. Zhu, D. A. Chesson, and Y. T. Yu, "Review—$(Mn,Co)_3O_4$ -based spinels for SOFC interconnect coating application." *J. Electrochem. Soc.*, **168**, 114519 (2021).
11. N. H. Menzler, D. Sebold, and O. Guillon, "Post-test characterization of a solid oxide fuel cell stack operated for more than 30,000 h: The cell." *J. Power Sources*, **374**, 69 (2018).
12. M. Hilger et al., "Towards sustainable interconnects for solid oxide cells: An integrated technical and environmental evaluation of coating methods." *J. Power Sources*, **659**, 238471 (2025).
13. L. Blum, U. Packbier, I. C. Vinke, and L. G. J. De Haart, "Long-term testing of SOFC stacks at Forschungszentrum Jülich." *Fuel Cells*, **13**, 646 (2013).
14. L. Blum, L. G. J. de Haart, J. Malzbender, N. Margaritis, and N. H. Menzler, "Anode-supported solid oxide fuel cell achieves 70 000 h of continuous operation." *Energy Technol*, **4**, 939 (2016).
15. N. Grünwald, D. Sebold, Y. J. Sohn, N. H. Menzler, and R. Vaßen, "Self-healing atmospheric plasma sprayed $Mn_{1.0}Co_{1.9}Fe_{0.1}O_4$ protective interconnector coatings for solid oxide fuel cells." *J. Power Sources*, **363**, 185 (2017).
16. M. Wolff, A. Schwiers, K. Wilkner, D. Sebold, and N. H. Menzler, "Wet powder spraying—a versatile and highly effective technique for the application of spinel-type protective coatings on SOC interconnects." *J. Power Sources*, **592**, 233931 (2024).

17. F. Tietz, Q. Fu, V. A. C. Haanappel, A. Mai, N. H. Menzler, and S. Uhlenbruck, "Materials development for advanced planar solid oxide fuel cells." *Int J Applied Ceramic Technology*, **4**, 436 (2007).
18. A. Petric and H. Ling, "Electrical conductivity and thermal expansion of spinels at elevated temperatures." *J American Ceramic Society*, **90**, 1515 (2007).
19. A. H. Tkaczyk, A. Bartl, A. Amato, V. Lapkovskis, and M. Petranikova, "Sustainability evaluation of essential critical raw materials: cobalt, niobium, tungsten and rare Earth elements." *J. Phys. D: Appl. Phys.*, **51**, 203001 (2018).
20. É. Lèbre et al., "The social and environmental complexities of extracting energy transition metals." *Nat. Commun.*, **11**, 4823 (2020).
21. Z. Zhu et al., "Comparison of Cu–Mn and Mn–Co spinel coatings for solid oxide fuel cell interconnects." *Int. J. Hydrogen Energy*, **47**, 36953 (2022).
22. S. N. Basu et al., "Electrophoretically deposited protective Cu-Mn and Mn-Co spinel coatings for solid oxide fuel cell interconnects." *In: ECS Transactions*, **111**, 2233 (2023).
23. K. Suo et al., "Processing and performance of protective Ni-doped Cu Mn spinel interconnect coatings." *Int. J. Refract. Met. Hard Mater*, **126**, 106947 (2025).
24. W. Huang, S. Gopalan, U. B. Pal, and S. Basu, "Evaluation of electrophoretically deposited $CuMn_{1.8}O_4$ spinel coatings on metallic interconnects for SOFC applications." *ECS Trans.*, **13**, 405 (2008).
25. Z. Sun et al., *Energy Technology* (The Minerals, Metals & Materials Series) 265 (2019).
26. H. Ling, "Electrical and thermal properties of spinels." *Proc Vol*, **2005–07**, 1866 (2005).
27. E. Zanchi, A. G. Sabato, S. Molin, G. Cempura, A. R. Boccaccini, and F. Smeacetto, "Recent advances on spinel-based protective coatings for solid oxide cell metallic interconnects produced by electrophoretic deposition." *Mater. Lett.*, **286**, 129229 (2021).
28. A. G. Sabato et al., "Mn-Co spinel coatings on Crofer 22 APU by electrophoretic deposition: Up scaling, performance in SOFC stack at 850 °C and compositional modifications." *J. Eur. Ceram. Soc.*, **41**, 4496 (2021).
29. S. I. Lee et al., "Highly dense Mn-Co spinel coating for protection of metallic interconnect of solid oxide fuel cells." *J. Electrochem. Soc.*, **161**, F1389 (2014).
30. B. Talic, H. Falk-Windisch, V. Venkatachalam, P. V. Hendriksen, K. Wiik, and H. L. Lein, "Effect of coating density on oxidation resistance and Cr vaporization from solid oxide fuel cell interconnects." *J. Power Sources*, **354**, 57 (2017).
31. E. Zanchi et al., "Manganese–cobalt based spinel coatings processed by electrophoretic deposition method: the influence of sintering on degradation issues of solid oxide cell oxygen electrodes at 750 °C." *Materials*, **14**, 3836 (2021).
32. VDM Metals. Crofer22APU Safety data sheet [Internet]. 2022 [cited 2025 Apr 13]. Available from: https://vdm-metals.com/fileadmin/user_upload/Downloads/Data_Sheets/Data_Sheet_VDM_Crofer_22_APU.pdf.
33. VDM Metals. Crofer22H Safety data sheet [Internet]. 2021 [cited 2025 Apr 13]. Available from: https://vdm-metals.com/fileadmin/user_upload/Downloads/Data_Sheets/Data_Sheet_VDM_Crofer_22_H.pdf.
34. F. Smeacetto et al., "Electrophoretic deposition of Mn1.5Co1.5O4 on metallic interconnect and interaction with glass-ceramic sealant for solid oxide fuel cells application." *J. Power Sources*, **280**, 379 (2015).
35. S. Molin et al., "Microstructural and electrical characterization of Mn-Co spinel protective coatings for solid oxide cell interconnects." *J. Eur. Ceram. Soc.*, **37**, 4781 (2017).
36. S. Molin, A. G. Sabato, H. Javed, G. Cempura, A. R. Boccaccini, and F. Smeacetto, "Co-deposition of CuO and $Mn_{1.5}Co_{1.5}O_4$ powders on Crofer22APU by electrophoretic method: Structural, compositional modifications and corrosion properties." *Mater. Lett.*, **218**, 329 (2018).
37. A. G. Sabato, S. Molin, H. Javed, E. Zanchi, A. R. Boccaccini, and F. Smeacetto, "In-situ Cu-doped MnCo-spinel coatings for solid oxide cell interconnects processed by electrophoretic deposition." *Ceram. Int.*, **45**, 19148 (2019).
38. M. Fakouri Hasanabadi, A. H. Kokabi, M. A. Faghihi-Sani, S. M. Groß-Barsnick, and J. Malzbender, "Room- and high-temperature torsional shear strength of solid oxide fuel/electrolysis cell sealing material." *Ceram. Int.*, **45**, 2219 (2019).
39. J. G. Grolig, H. Abdesselam, M. Gas, H. F. Windisch, J. Froitzheim, and J. E. Svensson, "Copper based conversion coatings on ferritic stainless strip steel as solid oxide fuel cell interconnects: oxidation performance and chromium evaporation." *ECS Trans.*, **57**, 2339 (2013).
40. J. Froitzheim, H. Ravash, E. Larsson, L. G. Johansson, and J. E. Svensson, "Investigation of chromium volatilization from FeCr interconnects by a denuder technique." *J. Electrochem. Soc.*, **157**, B1295 (2010).
41. J. G. Grolig, J. Froitzheim, and J. E. Svensson, "Coated stainless steel 441 as interconnect material for solid oxide fuel cells: Evolution of electrical properties." *J. Power Sources*, **284**, 321 (2015).
42. S. M. Gross, D. Federmann, J. Remmel, and M. Pap, "Reinforced composite sealants for solid oxide fuel cell applications." *J. Power Sources*, **196**, 7338 (2011).
43. D. Federmann, S. M. Groß-Barsnick, and H. R. Zerfass, "Forschungszentrum Jülich GmbH. Method for producing a solder glass green seal." *METHOD FOR PRODUCING A SOLDER GLASS GREEN SEAL*, EUEP 2 991 942 B1 (2014), 991942B1.
44. M. J. Reddy et al., "Experimental review of the performances of protective coatings for interconnects in solid oxide fuel cells." *J. Power Sources*, **568**, 232831 (2023).
45. A. Masi et al., "The effect of chemical composition on high temperature behaviour of Fe and Cu doped Mn-Co spinels." *Ceram. Int.*, **43**, 2829 (2017).
46. B. Wang, K. Li, J. Liu, T. Zhang, T. Yang, and N. Zhang, "Promoting electric conductivity of MnCo spinel coating by doping transition metals (Cu, Fe) or rare-Earth elements (La, Y) for solid oxide fuel cell interconnect." *Int. J. Hydrogen Energy*, **61**, 216 (2024).
47. I. Aznam, J. C. W. Mah, A. Muchtar, M. R. Somalu, and M. J. Ghazali, "Electrophoretic deposition of $(Cu,Mn,Co)_3O_4$ spinel coating on SUS430 ferritic stainless steel: Process and performance evaluation for solid oxide fuel cell interconnect applications." *J. Eur. Ceram. Soc.*, **41**, 1360 (2021).
48. Z. Sun, R. Wang, A. Y. Nikiforov, S. Gopalan, U. B. Pal, and S. N. Basu, "$CuMn_{1.8}O_4$ protective coatings on metallic interconnects for prevention of Cr-poisoning in solid oxide fuel cells." *J. Power Sources*, **378**, 125 (2018).
49. M. J. Reddy, T. E. Chausson, J. E. Svensson, and J. Froitzheim, "11–23% Cr steels for solid oxide fuel cell interconnect applications at 800 °C—How the coating determines oxidation kinetics." *Int. J. Hydrogen Energy*, **48**, 12893 (2023).
50. B. Talic, A. C. Wulff, S. Molin, K. B. Andersen, P. Zielke, and H. L. Frandsen, "Investigation of electrophoretic deposition as a method for coating complex shaped steel parts in solid oxide cell stacks." *Surf. Coat. Technol.*, **380**, 125093 (2019).